

Measurement of Absolute Transition Dipole Moment Functions of the $3^1\Pi \rightarrow 1(X)^1\Sigma^+$ and $3^1\Pi \rightarrow 2(A)^1\Sigma^+$ Transitions in NaK Using Autler-Townes Spectroscopy and Calibrated Fluorescence

S. J. Sweeney¹, E. H. Ahmed², P. Qi², T. Kirova^{2,*}, A. M. Lyyra², and J. Huennekens¹

¹Department of Physics, 16 Memorial Drive East, Lehigh University, Bethlehem, PA 18015

²Department of Physics, Temple University, Philadelphia, PA 19122-6082

Abstract

We describe a two-laser experiment using optical-optical double resonance fluorescence and Autler-Townes splittings to determine the NaK $3^1\Pi \rightarrow 1(X)^1\Sigma^+$, $2(A)^1\Sigma^+$ absolute transition dipole moment functions. Resolved $3^1\Pi \rightarrow A^1\Sigma^+$ and $3^1\Pi \rightarrow X^1\Sigma^+$ fluorescence was recorded with the frequencies of a Titanium-Sapphire laser (L1) and a ring dye laser (L2) fixed to excite particular $3^1\Pi(\nu=19, J=11, f) \leftarrow A^1\Sigma^+(\nu', J'=J=11, e) \leftarrow X^1\Sigma^+(\nu'', J''=J' \pm 1, e)$ double resonance transitions. The coefficients of a trial transition dipole moment function $\mu_e(R) = a_0 + a_1 \left(\frac{R_{eq}}{R}\right)^2 + a_2 \left(\frac{R_{eq}}{R}\right)^4 + \dots$ were adjusted to match the relative intensities of resolved spectral lines terminating on the lower $A^1\Sigma^+(\nu', 11, e)$ and $X^1\Sigma^+(\nu'', 11, e)$ levels. These data provide a *relative* measure of the functions $\mu_e(R)$ over a broad range of R . Next, L2 was tuned to either the $3^1\Pi(19, 11, f) \leftarrow A^1\Sigma^+(10, 11, e)$ or $3^1\Pi(19, 11, f) \leftarrow A^1\Sigma^+(9, 11, e)$ transition and

*Current address: Laser Centre, Faculty of Physics and Mathematics, University of Latvia, Riga, Latvia

focused to an intensity large enough to split the levels via the Autler-Townes (AT) effect. L1 was scanned over the $A^1\Sigma^+(10,11,e) \leftarrow X^1\Sigma^+(1,10,e)$ or $A^1\Sigma^+(9,11,e) \leftarrow X^1\Sigma^+(0,12,e)$ transition to probe the AT lineshape, which was fit using density matrix equations to yield an *absolute* value for $\mu_{ik} = \int \psi_{vib}^i(R) \mu_e(R) \psi_{vib}^k(R) dR$ where i and k represent the upper and lower levels, respectively, of the coupling laser (L2) transition. Finally, the values of μ_{ik} were used to place the relative $\mu_e(R)$ functions obtained with resolved fluorescence onto an absolute scale. We compare our experimental transition dipole moment functions to the theoretical work of Magnier *et al.* [1].

I. Introduction

One-photon absorption spectra of transitions between two electronic states of alkali diatomic molecules are exceedingly complex due to both the small vibrational and rotational constants and the fact that a large number of rovibrational levels in the electronic ground state are thermally populated at the temperatures used (generally 300-400°C in the case of NaK). The intricacy of the absorption spectra can be avoided with the use of optical-optical double resonance (OODR) spectroscopy [2-8]. A pump laser is first used to excite a specific rovibrational transition from a thermally populated level in the electronic ground state to a level in an intermediate electronic state. A second laser, labeled the probe, is then used to excite the molecules in the initially excited intermediate state to a rovibrational level in a higher excited electronic state. Fluorescence from this upper level can be used to monitor the absorption of the probe laser photons. In other cases, fluorescence from nearby collisionally populated levels of the same or another electronic state, fluorescence from atomic levels populated through predissociation or collisional energy-transfer processes, ionization signals produced by collisions or

photoionization involving molecules in the upper level, or a change in the state of polarization of the transmitted probe laser beam can be used to monitor the OODR transition. The spectra produced by these methods are much simpler to analyze when compared to one-photon absorption spectra. This is due to the fact that the starting point for the laser transitions is a single rovibrational level in the ground state, as compared to hundreds of thermally populated rovibrational levels. If narrow-band lasers are used, the OODR spectra are also Doppler-free.

If the fluorescence from the upper excited state level is resolved with a monochromator, the specific transitions from the upper level to each rovibrational level in lower electronic states can be measured. The relative intensities of these peaks, when corrected for detection system efficiencies, can be fit to provide a relative electronic transition dipole moment function $\mu_e(R)$. These results can be used to test theoretical calculations [1,9], albeit only in terms of the *relative* dependence of $\mu_e(R)$ on R . To also test the magnitude of $\mu_e(R)$, a measurement of the absolute transition dipole moment between two states must be made. Recently, it has been shown that this type of measurement can be made in molecular systems by utilizing the Autler-Townes effect [10-15].

It has been shown [10-24] that the Autler-Townes effect can be used in three- and four-level systems to measure absolute values of transition dipole matrix elements between rovibrational levels in homonuclear diatomic molecules and to make possible all-optical control of molecular angular momentum alignment. In the present work, we used a three-level scheme to measure the absolute transition dipole matrix elements between specific levels of the $3^1\Pi$ and $2(A)^1\Sigma^+$ electronic states of NaK. These results were then used to place the relative $3^1\Pi \rightarrow 2(A)^1\Sigma^+$ and $3^1\Pi \rightarrow 1(X)^1\Sigma^+$ transition dipole moment functions obtained from calibrated

fluorescence onto an absolute scale. In the present case, the transition dipole moment functions vary rapidly with internuclear separation. In addition, the dipole matrix elements are not large, even in the most favorable cases. Thus only a few transition matrix elements can be measured with the AT splitting method. However, the combination of AT splitting with calibrated fluorescence allows a complete mapping of the transition dipole moment functions over fairly broad ranges of R .

II. Experiment

a) Experimental Setup – OODR Resolved Fluorescence

The experimental setup is shown in Figure 1, and is similar to the one described in Laub *et. al* [25]. The sodium-potassium mixture is contained in a six-arm cross-type heat-pipe oven, maintained at a temperature in the range 332-365°C and containing argon as a buffer gas ($P = 0.15 - 1.5$ Torr). A single-mode Ti:Sapphire laser (Coherent model 899-29), labeled L1 in Fig. 1, is pumped by a 10W argon ion laser and produces 300 - 700 mW in the wavelength range 730 - 850 nm. It is used as the pump laser in the OODR pumping scheme to excite a specific $A^1\Sigma^+(v', J = 11, e) \leftarrow X^1\Sigma^+(v'', J \pm 1, e)$ transition (see Fig. 2a). A single-mode ring dye laser (Coherent model 699-29), labeled L2, is pumped by a 4W krypton ion laser and produces $\sim 200 - 500$ mW of tunable power in the wavelength range 725 - 775 nm using LD700 dye. L2 serves as the probe laser, and is tuned to the $3^1\Pi(19, 11, f) \leftarrow A^1\Sigma^+(v', 11, e)$ transition. The two lasers counterpropagate through the heat-pipe oven, producing Doppler-free excitation lines.

The pump laser frequency is set to line-center of a specific $A^1\Sigma^+(v', J' = 11, e) \leftarrow X^1\Sigma^+(v'', J'' = J' \pm 1, e)$ transition by monitoring the total $A^1\Sigma^+ \rightarrow X^1\Sigma^+$ fluorescence from the heat-pipe with only the pump laser entering the oven. The red

fluorescence emitted at right angles to the laser propagation direction is detected with a free-standing photomultiplier tube (Hamamatsu R406) outfitted with a 700-1000nm interference filter (“Total Red PMT” in Fig. 1). The probe laser is scanned over the $3^1\Pi(19,11,f) \leftarrow A^1\Sigma^+(v',11,e)$ transition, and its frequency is set by monitoring the total $3^1\Pi \rightarrow X^1\Sigma^+$ fluorescence using a second freestanding PMT (Hamamatsu R928) outfitted with a set of three interference filters chosen to pass light in the 353-462nm range. This “Total Violet PMT” collects fluorescence on the opposite side of the heat-pipe oven from the Total Red PMT, as shown in Fig. 1.

The removal of a mirror from the fluorescence path to the Total Red PMT allows for resolved $3^1\Pi(19,11,f) \rightarrow X^1\Sigma^+(v'',11,e)$ and $3^1\Pi(19,11,f) \rightarrow A^1\Sigma^+(v',11,e)$ fluorescence scans to be taken with a 0.33m monochromator outfitted with a Hamamatsu R1387 PMT. These scans were recorded with both laser frequencies fixed to the line-centers of their respective transitions. Lasers L1 and L2 were chopped at different frequencies f_1 and f_2 using a dual frequency chopper (Stanford Research Systems model SR540) and signals were processed by a digital lock-in amplifier (SR850) locked to the sum frequency $f_1 + f_2$. This was necessary in order to distinguish the $3^1\Pi(19,11,f) \rightarrow A^1\Sigma^+(v',11,e)$ fluorescence from the single-laser (L1 or L2) induced background light in the same frequency range. Recorded signals from the Total Violet PMT were used to correct relative resolved peak intensities for small frequency and power fluctuations associated with either laser.

A second removable mirror on the Total Violet PMT side of the heat pipe (not shown in Fig. 1) was used to send light from a calibrated tungsten-halogen white light source through the heat pipe and into the monochromator, allowing for calibration of the relative wavelength-dependent response of the detection system [26]. The polarization dependence of the detection

system (for light linearly polarized either parallel or perpendicular to the grating grooves) was determined by fitting a linear polarizer to the monochromator entrance slit in different orientations and taking additional white light scans. The polarization of the resolved lines was also measured with the same linear polarizer. These results were used to correct the measured fluorescence line intensities. Finally, white light scans recorded when the oven was hot allowed us to correct the fluorescence line intensities for attenuation due to the relatively small (except at the potassium resonance lines) absorption of fluorescence photons by the alkali vapor in the fluorescence arms of the heat pipe.

b) Experimental Setup – AT Splitting

The experimental setup for probing the AT splitting lineshapes is essentially the same as for the OODR fluorescence measurements, with just a few exceptions. The Ti:Sapphire laser (L1, now called the probe laser) and dye laser (L2, now called the coupling laser) frequencies were set to line center of their respective transitions as described above. Three lenses were inserted into each beam path to focus the probe and coupling laser beam radii to 120-135 μm and 330-345 μm , respectively. The smaller spot size of the probe beam was chosen so that the electric field of the coupling laser could be considered to be spatially uniform over the probe region. The probe laser passed through a set of neutral density filters (Schott glass NG-3, 4, and 9) to attenuate the power to $< 1\text{mW}$ in order to minimize power broadening. The coupling laser power was maintained between 240-430mW to maximize the splitting of the fluorescence lines due to the Autler-Townes effect. The electric field of the coupling laser was measured using a power meter and razor blades mounted to an x-y translator as described in Ref. [27]. Great care was taken to insure the proper spatial overlap of the beam profiles at the center of the oven.

With the coupling laser fixed to the $3^1\Pi(19,11,f) \leftarrow A^1\Sigma^+(v',11,e)$ transition, the probe laser was scanned over the $A^1\Sigma^+(v',J'=11,e) \leftarrow X^1\Sigma^+(v'',J'\pm 1,e)$ transition, and the total violet fluorescence was recorded (see Fig. 2b). The probe laser frequency dependence of this signal maps out the Autler-Townes lineshape (see Ref. [15]).

III. Resolved Fluorescence

Figures 3 and 4 show examples of the recorded $3^1\Pi(19,11,f) \rightarrow A^1\Sigma^+(v',11,e)$ and $3^1\Pi(19,11,f) \rightarrow X^1\Sigma^+(v'',11,e)$ fluorescence spectra, respectively. It can be seen that the $3^1\Pi(19,11,f) \rightarrow X^1\Sigma^+(v'',11,e)$ fluorescence, which occurs in the violet part of the spectrum, is quite clean and is recorded with excellent signal-to-noise even for the weak lines. However, the red $3^1\Pi(19,11,f) \rightarrow A^1\Sigma^+(v',11,e)$ fluorescence appears in a very congested part of the spectrum, where both lasers pump a number of $A^1\Sigma^+ \leftarrow X^1\Sigma^+$ transitions of NaK and K_2 leading to strong $A^1\Sigma^+ \rightarrow X^1\Sigma^+$ fluorescence bands in addition to the NaK $3^1\Pi \rightarrow A^1\Sigma^+$ fluorescence of interest. Even with modulation of both lasers and lock-in detection at the sum frequency $f_1 + f_2$, the spectrum is still quite congested and noisy. However, we could pump the $3^1\Pi(19,11,f)$ level using different pump/probe excitation paths, and in each case it was possible to pick out several NaK $3^1\Pi \rightarrow A^1\Sigma^+$ fluorescence lines since they are separated by the known $A^1\Sigma^+$ state vibrational and rotational intervals and since extraneous lines would not appear in all of the spectra obtained with different excitation schemes. In Fig. 3, one such spectrum is shown. NaK $3^1\Pi \rightarrow A^1\Sigma^+$ fluorescence lines are marked by vertical arrows. The horizontal arrow marks the region where potassium resonance line absorption drastically reduces the transmission of the

vapor. Nonetheless, relative intensities of eleven different $3^1\Pi(19,11,f) \rightarrow A^1\Sigma^+(v',11,e)$ transitions [including the $3^1\Pi(19,11,f) \rightarrow A^1\Sigma^+(10,11,e)$ and $3^1\Pi(19,11,f) \rightarrow A^1\Sigma^+(9,11,e)$ transitions that serve as the absolute AT splitting calibration lines] were successfully recorded. With the white light measurements of the relative detection system efficiency vs. wavelength, all of the $3^1\Pi(19,11,f) \rightarrow A^1\Sigma^+(v',11,e)$ and $3^1\Pi(19,11,f) \rightarrow X^1\Sigma^+(v'',11,e)$ fluorescence line intensities could be put on the same relative intensity scale.

Theoretically, since all observed fluorescence transitions are $^1\Pi \rightarrow ^1\Sigma^+$ Q lines, the relative intensities of the peaks in the resolved NaK $3^1\Pi(19,11,f) \rightarrow A^1\Sigma^+(v',11,e)$ and $3^1\Pi(19,11,f) \rightarrow X^1\Sigma^+(v'',11,e)$ fluorescence scans are given by [28]

$$I_{fluor} \propto \nu_{ik}^4 |\mu_{ik}|^2, \quad (1)$$

where i and k represent the upper and lower levels of the transition, respectively, and the transition dipole matrix element μ_{ik} is $\mu_{ik} = \int \psi_{vib}^i(R) \mu_e(R) \psi_{vib}^k(R) dR$. For the electronic transition dipole moment function $\mu_e(R)$, a polynomial of the form

$$\mu_e(R) = a_0 + a_1 \left(\frac{R_{eq}}{R} \right)^2 + a_2 \left(\frac{R_{eq}}{R} \right)^4 + \dots \quad (2)$$

with fitting parameters $a_0, a_1, a_2 \dots$ was used to fit the calculated intensities to the experimental intensities. Here, $R_{eq} = 4.4587 \text{ \AA}$ is the equilibrium internuclear separation of the $3^1\Pi$ state. We used the computer program LEVEL 8.0 [29], to calculate the matrix elements of the terms $(R_{eq}/R)^n$ for the measured transitions between the $3^1\Pi(19,11,f)$ level and the various $A^1\Sigma^+(v',11,e)$ and $X^1\Sigma^+(v'',11,e)$ levels. In these calculations, the experimental potentials of

Laub *et al.* [25], Ross *et al.* [30], and Russier-Antoine *et al.* [31] were used for the $3^1\Pi$, $A^1\Sigma^+$, and $X^1\Sigma^+$ states, respectively.

To determine the best values for the constants a_i for the $3^1\Pi \rightarrow A^1\Sigma^+$ and $3^1\Pi \rightarrow X^1\Sigma^+$ transition dipole moment functions, we used the non-linear fitting tool in Origin 7.5 to fit the experimentally measured intensities from the resolved fluorescence spectra. The experimental data were assigned a statistical weighting; i.e., each transition peak was assigned the same percent error. To determine the best fit, Origin minimizes the reduced chi-squared. The number of fitting parameters was varied, and the best fit was taken to be the one with the lowest reduced chi-squared. With too many parameters, the reduced chi-squared increases, and the errors in the parameters of the highest order terms also become larger than the parameters themselves. The best fit of the $3^1\Pi(19,11,f) \rightarrow A^1\Sigma^+(v',11,e)$ spectra included two terms (a_0 and a_1), while four terms (a_1 , a_2 , a_3 , and a_4) yielded the best fit to the $3^1\Pi(19,11,f) \rightarrow X^1\Sigma^+(v'',11,e)$ spectra. The a_0 term was excluded from the $3^1\Pi \rightarrow X^1\Sigma^+$ transition dipole moment function, since this function is expected to go to zero at large R . This is due to the fact that while the molecular transition is allowed, the atomic transition $\text{Na}(3S) + \text{K}(3D) \rightarrow \text{Na}(3S) + \text{K}(4S)$ is dipole forbidden (as $R \rightarrow \infty$). Note that, as in the work of Laub *et al.* [25], this fitting of relative intensities provides only relative transition dipole moment functions.

IV. Autler-Townes Splitting - Theory and Analysis

We model the present cascade-style Autler-Townes experiment as a closed five-level system, as shown in Fig. 5. Levels 1, 3 and 5 are the initial, intermediate, and final states of the

two-laser OODR pump scheme. The strong coupling laser L2 is fixed to line center of the $3 \rightarrow 5$ transition, and the strength of the coupling is described by the Rabi frequency

$$\Omega_{35} = \mu_{35} E_{L2} / \hbar = \langle 3^1\Pi(19,11,f) | \mu_{e,3^1\Pi \rightarrow A^1\Sigma^+}(R) | A^1\Sigma^+(v',11,e) \rangle E_{L2} / \hbar, \quad (3)$$

where E_{L2} is the electric field of the coupling laser. The weak probe laser L1 is scanned over the $1 \rightarrow 3$ transition, and the relevant Rabi frequency is Ω_{13} . Levels 2 and 6 represent all other NaK rovibrational levels that can be populated by radiative decay from levels 3 and 5. Specifically, level 6 consists of all $A^1\Sigma^+$ and other electronic state rovibrational levels, except level 3 and levels of the $X^1\Sigma^+$ ground state, that are radiatively coupled to level 5. Level 2 consists of all $X^1\Sigma^+$ levels except level 1.

To simulate the AT lineshape, we must solve the density matrix equations of motion including both the effects of the rovibrational magnetic sublevels (M_J) and the motion of the molecules along the laser propagation direction (Doppler shifts) and transverse to the laser propagation direction (transit relaxation). Transit relaxation must be included here because the transit rate is comparable to the radiative decay rates. The density matrix equations can be written as [23, 32]

$$\dot{\rho}_{nm} = -\frac{i}{\hbar} \sum_k (H_{nk} \rho_{km} - \rho_{nk} H_{km}) + \text{relaxation terms} \quad (4)$$

where ρ_{nm} is a density matrix element. Diagonal terms ρ_{ii} represent the level populations, while off-diagonal elements ρ_{ij} describe coherences. Relaxation terms include collisional and radiative transfer of population, transit relaxation, and collisional decoherence (line broadening). The H_{ij} are the matrix elements of the Hamiltonian, which is given by

$$\begin{aligned}
\mathbf{H} = & \hbar\omega_{21}|2\rangle\langle 2| + \hbar\omega_{31}|3\rangle\langle 3| + \hbar\omega_{51}|5\rangle\langle 5| + \hbar\omega_{61}|6\rangle\langle 6| \\
& + \frac{\hbar\Omega_{13}}{2}(|3\rangle\langle 1| + |1\rangle\langle 3|) + \frac{\hbar\Omega_{35}}{2}(|5\rangle\langle 3| + |3\rangle\langle 5|).
\end{aligned} \tag{5}$$

Because levels 1 and 3 and levels 3 and 5 are coupled by lasers, the 1-3 and 3-5 off-diagonal terms are not zero. We can write the individual terms of the Hamiltonian matrix:

$$\begin{aligned}
H_{11} &= 0 \\
H_{22} &= \hbar\omega_{21} \\
H_{33} &= \hbar\omega_{31} \\
H_{55} &= \hbar\omega_{51} \\
H_{66} &= \hbar\omega_{61} \\
H_{13} = H_{31} &= \frac{\hbar\Omega_{13}}{2} \\
H_{35} = H_{53} &= \frac{\hbar\Omega_{35}}{2},
\end{aligned} \tag{6}$$

where $\omega_{i1} = (E_i - E_1)/\hbar$ is the angular frequency associated with the energy gap between level i and level 1. Since we use cw lasers in our experiment, we can assume that the populations of all levels are constant in time; $\dot{\rho}_{ii} = 0$.

In our model, we assume that levels 3, 5, and 6 decay by spontaneous emission and transit relaxation, while levels 1 and 2 only decay by transit relaxation. We assume that levels 3 and 6 decay only to levels 1 and 2, while level 5 decays to 1, 2, 3, and 6. This assumption regarding level 6 is valid since level 6 consists primarily of rovibrational levels of the $A^1\Sigma^+$ and $B^1\Pi$ states, which radiate either not at all or only weakly to level 3. We can write the density matrix equation of motion for the population in sublevel 3, $M_J = M$ as

$$\dot{\rho}_{33}^{MM} = 0 = -(\Gamma_3 + \Gamma_t) \rho_{33}^{MM} + \sum_{\alpha=-1}^1 \Gamma_{5(M+\alpha),3M} \rho_{55}^{M+\alpha,M+\alpha} - \frac{i\Omega_{13}^{MM}}{2} (\rho_{13}^{MM} - \rho_{31}^{MM}) - \frac{i\Omega_{35}^{MM}}{2} (\rho_{53}^{MM} - \rho_{35}^{MM}). \quad (7)$$

In this expression, Γ_i , $\Gamma_{i,j}$, and Γ_t represent the total spontaneous decay rate out of level i , the decay rate from level i to level j , and the transit relaxation rate, respectively. The last two terms on the right hand side represent the coupling of level 1, M to 3, M and level 3, M to 5, M due to the interaction of the molecules with lasers L1 and L2, respectively. Since both lasers are linearly polarized, we only create coherences between levels with the same magnetic quantum number M . Spontaneous emission couples higher and lower state sublevels of different M according to the dipole selection rule $\Delta M = 0, \pm 1$. However, if we invoke an approximation introduced by Spano [23] that the populations in three neighboring M levels are approximately equal (this approximation is valid for systems with strong pumping), then we can write

$$\sum_{\alpha=-1}^1 \Gamma_{i(M+\alpha),jM} \rho_{ii}^{M+\alpha,M+\alpha} \approx \rho_{ii}^{MM} \sum_{\alpha=-1}^1 \Gamma_{i(M+\alpha),jM} = \rho_{ii}^{MM} \Gamma_{ij}, \quad (8)$$

and Eq. (7) becomes

$$\dot{\rho}_{33}^{MM} = 0 = -(\Gamma_3 + \Gamma_t) \rho_{33}^{MM} + \Gamma_{53} \rho_{55}^{MM} - \frac{i\Omega_{13}^{MM}}{2} (\rho_{13}^{MM} - \rho_{31}^{MM}) - \frac{i\Omega_{35}^{MM}}{2} (\rho_{53}^{MM} - \rho_{35}^{MM}). \quad (9)$$

In a similar manner, and again invoking Eq. (8), we can write the density matrix equations for the other diagonal elements as follows [33]:

$$\dot{\rho}_{66}^{MM} = 0 = -(\Gamma_6 + \Gamma_t) \rho_{66}^{MM} + \Gamma_{56} \rho_{55}^{MM} \quad (10)$$

$$\dot{\rho}_{55}^{MM} = 0 = -(\Gamma_5 + \Gamma_t) \rho_{55}^{MM} - \frac{i\Omega_{35}^{MM}}{2} (\rho_{35}^{MM} - \rho_{53}^{MM}) \quad (11)$$

$$\dot{\rho}_{22}^{MM} = 0 = -\Gamma_t (\rho_{22}^{MM} - \rho_{22e}^{MM}) + \Gamma_{32} \rho_{33}^{MM} + \Gamma_{52} \rho_{55}^{MM} + \Gamma_{62} \rho_{66}^{MM} \quad (12)$$

and

$$\begin{aligned}
\dot{\rho}_{11}^{MM} = 0 &= -\Gamma_t (\rho_{11}^{MM} - \rho_{11e}^{MM}) + \Gamma_{31} \rho_{33}^{MM} + \Gamma_{51} \rho_{55}^{MM} + \Gamma_{61} \rho_{66}^{MM} - \frac{i\Omega_{13}^{MM}}{2} (\rho_{31}^{MM} - \rho_{13}^{MM}) \\
&= \Gamma_t (\rho_{22}^{MM} - \rho_{22e}^{MM}) + [\Gamma_{31} + \Gamma_t] \rho_{33}^{MM} + [\Gamma_{51} + \Gamma_t] \rho_{55}^{MM} + [\Gamma_{61} + \Gamma_t] \rho_{66}^{MM} \\
&\quad - \frac{i\Omega_{13}^{MM}}{2} (\rho_{31}^{MM} - \rho_{13}^{MM})
\end{aligned} \tag{13}$$

where we have defined the equilibrium populations in levels 1, M and 2, M to be ρ_{11e}^{MM} and ρ_{22e}^{MM} , respectively, and used the conservation equation

$$\sum_i \rho_{ii}^{MM} = \rho_{11e}^{MM} + \rho_{22e}^{MM} = 1/g \tag{14}$$

(here g is the number of different M levels pumped by the laser). Thus, transit relaxation tends to restore the populations in levels 1, M and 2, M to their equilibrium values.

Driving terms associated with external laser fields are represented by off-diagonal density matrix elements ρ_{ij} . The density matrix equations for the time development of these off-diagonal elements also follow from Eq. (4). Following Spano [23] we can write the electric field of a linearly polarized laser beam as

$$\vec{E}_L = \frac{1}{2} \left[E_L \hat{\epsilon} e^{-i\omega_L t} + (E_L \hat{\epsilon})^* e^{i\omega_L t} \right], \tag{15}$$

where ω_L is the frequency of the laser in question and $\hat{\epsilon}$ is the polarization unit vector. In this experiment, the laser frequencies are either exactly on, or very near to resonance in all cases. Therefore, one term in Eq. (15) will lead to density matrix elements that are slowly varying while the other will create terms oscillating at frequencies of $\sim 2\omega_L$. The rotating wave approximation consists of neglecting the rapidly oscillating off-diagonal terms (at frequencies such as $\omega_{L2} + \omega_{53}$) compared to the nearly resonant terms (such as $\omega_{L2} - \omega_{53}$). This approximation

allows us to write the off-diagonal density matrix element ρ_{ij} in terms of a slowly varying quantity σ_{ij} :

$$\rho_{ij} = \sigma_{ij} e^{-i(\omega_L - k_L v_z)t} \quad (16)$$

where $(\omega_L - k_L v_z)$ is the Doppler shifted laser frequency in the rest frame of the molecule, $\bar{k}_L = (\omega_L/c)\hat{z}$ is the laser wavevector, and v_z is the component of the molecular velocity along the laser L1 propagation direction. Note that for counterpropagating lasers, as used in this experiment, k_{L2} is negative.

Invoking the rotating wave approximation, the equation for $\dot{\rho}_{13}^{MM}$ is [23,33]:

$$\begin{aligned} \dot{\rho}_{31}^{MM} = & -i(\omega_{L1} - k_{L1}v_z)\rho_{31}^{MM} = -(\delta_{13} + \Gamma_t)\rho_{31}^{MM} + \frac{i\Omega_{13}^{MM}}{2}(\rho_{33}^{MM} - \rho_{11}^{MM}) \\ & - \frac{i}{\hbar}\hbar\omega_{31}\rho_{31}^{MM} - \frac{i\Omega_{35}^{MM}}{2}\rho_{51}^{MM}, \end{aligned} \quad (17)$$

which can be rewritten in the form

$$0 = -(i\Delta_{31} + \delta_{13} + \Gamma_t)\rho_{31}^{MM} + \frac{i\Omega_{13}^{MM}}{2}(\rho_{33}^{MM} - \rho_{11}^{MM}) - \frac{i\Omega_{35}^{MM}}{2}\rho_{51}^{MM}. \quad (18)$$

Similarly, the equations for $\dot{\rho}_{53}^{MM}$ and $\dot{\rho}_{51}^{MM}$ yield

$$0 = [-i\Delta_{53} - (\delta_{35} + \Gamma_t)]\rho_{53}^{MM} + \frac{i\Omega_{13}^{MM}}{2}\rho_{51}^{MM} - \frac{i\Omega_{35}^{MM}}{2}(\rho_{33}^{MM} - \rho_{55}^{MM}) \quad (19)$$

and

$$0 = [-i(\Delta_{53} + \Delta_{31}) - (\delta_{15} + \Gamma_t)]\rho_{51}^{MM} + \frac{i\Omega_{13}^{MM}}{2}\rho_{53}^{MM} - \frac{i\Omega_{35}^{MM}}{2}\rho_{31}^{MM}, \quad (20)$$

respectively. In these expressions, the velocity dependent detunings of lasers L1 and L2 are defined by $\Delta_{31} \equiv \omega_{31} - \omega_{L1} + k_{L1}v_z$ and $\Delta_{53} \equiv \omega_{53} - \omega_{L2} + k_{L2}v_z$, and $\delta_{ij} = \frac{1}{2}[\Gamma_i + \Gamma_j] + \gamma_{ij}^c$ is the

decay rate of the coherence between levels i and j . Here γ_{ij}^c is the collisional rate of decay of the coherence between levels, or the collisional line broadening rate (half-width at half maximum in angular frequency units). The off-diagonal density matrix elements are complex, and obey $\rho_{ij} = (\rho_{ji})^*$.

Equations (18) – (20) and their complex conjugates, combined with Eqs. (9) – (12) [note that Eq. (13) is not independent of (9) – (12)], plus the conservation equation (14), form a set of eleven coupled equations for the eleven density matrix elements ρ_{11}^{MM} , ρ_{22}^{MM} , ρ_{33}^{MM} , ρ_{55}^{MM} , ρ_{66}^{MM} , ρ_{13}^{MM} , ρ_{31}^{MM} , ρ_{15}^{MM} , ρ_{51}^{MM} , ρ_{35}^{MM} , and ρ_{53}^{MM} . In the experiment, we fix the coupling laser L2 to line center of the $3 \rightarrow 5$ transition, and scan the probe laser L1 over the $1 \rightarrow 3$ transition while monitoring $3^1\Pi(19, 11, f) \rightarrow X^1\Sigma^+$ violet fluorescence ($5 \rightarrow 1, 2$ fluorescence). Thus the measured signal is proportional to the total level 5 population, $\sum_M \rho_{55}^{MM}$. Although the Spano approximation [Eq. (8)] uncouples the equations for each different M value, the sets of equations for different M are not identical because the Rabi frequencies are M dependent. Specifically, we find

$$\begin{aligned}
\Omega_{ij}^{MM} &= \langle i, M | \mu_e(R) | j, M \rangle E_L / \hbar \\
&= F(i, M; j, M) \langle i | \mu_e(R) | j \rangle E_L / \hbar \\
&\equiv F(i, M; j, M) \Omega_{ij},
\end{aligned} \tag{21}$$

where $F(i, M; j, M)$ is Spano's transition dipole moment orientation factor. Spano [23] gives formulas for the $F(i, M; j, M)$ which depend on the type of electronic transition (e.g. $^1\Pi \leftrightarrow ^1\Sigma^+$

or $^1\Sigma^+ \leftrightarrow ^1\Sigma^+$), whether the rotational quantum number changes by -1 , 0 or $+1$ (P, Q or R transition), and on the M value.

We used a computer code that is a modified version of a program written by Kirova [34] in collaboration with Spano to model a three-laser experiment in Na_2 . The user inputs the measured electric fields and beam radii of the lasers L1 and L2, the Rabi frequencies Ω_{13} and Ω_{35} , and the collisional dephasing rates γ_{13}^c , γ_{15}^c , and γ_{35}^c . For known electric field strengths, Γ_{31} and Γ_{53} are not independent of Ω_{13} and Ω_{35} since both only depend on the dipole matrix elements. The calculations are not very sensitive to the various other radiative rates, which are all known fairly well from theory. The transit relaxation rate Γ_t was calculated using Eq. (8) in Sagle *et al.* [35]. In the experiment, the probe laser frequency is scanned. Therefore, the program loops over the Maxwell-Boltzmann distribution of velocities, v_z , calculates ρ_{55}^{MM} for each value of M , and reports $\rho_{55} \equiv \sum_M \rho_{55}^{MM}$ for each detuning of the probe laser L1. The output is the predicted Autler-Townes lineshape (see Fig. 6).

The predicted A-T lineshape displays two peaks, in general agreement with experiment. The splitting between the peaks is mostly determined by the Rabi frequency Ω_{35} of the coupling laser L2 which causes levels 3 and 5 to each split into two levels (Autler-Townes splitting). Ideally, the probe laser L1 should be sufficiently weak that the lineshape is independent of Ω_{13} . However, signal-to-noise issues required us to use L1 laser intensities such that the fitting was not entirely independent of Ω_{13} . We calculated Ω_{13} from the weighted average of the L1 electric field over the interaction region and the transition dipole matrix element obtained from LEVEL [29] using the theoretical transition dipole moment function of Magnier *et al.* [1]. The

collisional dephasing (line-broadening) rates γ_{13}^c , γ_{15}^c , and γ_{35}^c are found to strongly affect the widths of the peaks and the line wings, but to have relatively little effect on the splitting. Thus we varied Ω_{35} until the splitting of the calculated lineshape agreed with experiment, and then we adjusted the collisional dephasing rates to improve the agreement with the overall lineshape. Tests showed that varying Ω_{13} by $\pm 25\%$ results in $\pm 6\text{-}7\%$ shifts of the fitted values of Ω_{35} , while variation of γ_{13}^c , γ_{15}^c , and γ_{35}^c by $\pm 50\%$ typically affect Ω_{35} at the 6% level or less.

Finally, the transition dipole matrix element for the $3 \leftrightarrow 5$ transition could be obtained from the measured electric field (weighted average over the interaction region = 0.94 of the peak field) and the fitted Rabi frequency of the coupling laser:

$$\Omega_{35} = \frac{\mu_{35} E_{L2}}{\hbar}. \quad (22)$$

From Eq. (22) it can be seen that the Rabi frequency (and therefore the splitting between the two peaks of the lineshape) should vary with the square root of the coupling laser intensity. This is shown in Fig. 7. Using the measured electric field of the coupling laser and the best fitted values of the Rabi frequencies for the $3^1\Pi(19, 11, f) \leftarrow A^1\Sigma^+(10, 11, e)$ and $3^1\Pi(19, 11, f) \leftarrow A^1\Sigma^+(9, 11, e)$ transitions, we obtained $\mu_{3^1\Pi(19,11,f)\leftarrow A^1\Sigma^+(10,11,e)} = (1.51 \pm 0.15)$ Debye and $\mu_{3^1\Pi(19,11,f)\leftarrow A^1\Sigma^+(9,11,e)} = (0.90 \pm 0.09)$ Debye.

V. Results and Discussion

Several NaK $3^1\Pi(19,11,f) \rightarrow A^1\Sigma^+(v',11,e)$ and $3^1\Pi(19,11,f) \rightarrow X^1\Sigma^+(v'',11,e)$ resolved fluorescence scans were recorded and calibrated as described in Sec. III. The white light calibration of the relative detection system efficiency versus wavelength allowed us to put

all fluorescence line intensities on the same relative scale. The relative $3^1\Pi \rightarrow A^1\Sigma^+$ and $3^1\Pi \rightarrow X^1\Sigma^+$ transition dipole moment functions, $\mu_{e,3^1\Pi \rightarrow A^1\Sigma^+}^{relative}(R)$ and $\mu_{e,3^1\Pi \rightarrow X^1\Sigma^+}^{relative}(R)$, were modeled according to Eq. (2) and theoretical line intensities were calculated using Eq. (1). The parameters a_i were adjusted to give the best agreement with the measured $3^1\Pi(19,11,f) \rightarrow A^1\Sigma^+(v',11,e)$ and $3^1\Pi(19,11,f) \rightarrow X^1\Sigma^+(v'',11,e)$ line intensities. As stated above, a two parameter fit (a_0 and a_1) gave the best fit for the $3^1\Pi(19,11,f) \rightarrow A^1\Sigma^+(v',11,e)$ fluorescence while a four parameter fit (a_1 , a_2 , a_3 and a_4) yielded the best fit for the violet $3^1\Pi(19,11,f) \rightarrow X^1\Sigma^+(v'',11,e)$ fluorescence. A comparison between the experimental and fitted intensities is shown in Figs. 8 and 9 for the $3^1\Pi \rightarrow A^1\Sigma^+$ and $3^1\Pi \rightarrow X^1\Sigma^+$ fluorescence, respectively. Since the measured intensities are relative rather than absolute, the units of $\mu_{e,3^1\Pi \rightarrow A^1\Sigma^+}^{relative}(R)$ and $\mu_{e,3^1\Pi \rightarrow X^1\Sigma^+}^{relative}(R)$ are still arbitrary at this point.

We define a normalization factor N to scale the relative $\mu_e^{relative}(R)$ functions, and put them on an absolute scale. The AT splitting experiment yielded absolute transition dipole matrix elements, $\mu_{3^1\Pi(19,11,f) \leftarrow A^1\Sigma^+(10,11,e)}$ and $\mu_{3^1\Pi(19,11,f) \leftarrow A^1\Sigma^+(9,11,e)}$, for two specific transitions $3^1\Pi(19, 11, f) \leftarrow A^1\Sigma^+(10, 11, e)$ and $3^1\Pi(19, 11, f) \leftarrow A^1\Sigma^+(9, 11, e)$, respectively. We used the program LEVEL 8.0 [29] to calculate the transition dipole matrix elements $\mu_{3^1\Pi(19,11,f) \leftarrow A^1\Sigma^+(10,11,e)}$ and $\mu_{3^1\Pi(19,11,f) \leftarrow A^1\Sigma^+(9,11,e)}$ using the relative electronic transition dipole moment function $\mu_{e,3^1\Pi \rightarrow A^1\Sigma^+}^{relative}(R)$ obtained from resolved fluorescence. Comparison of these results with the absolute transition dipole matrix elements from the AT splitting experiment then yielded two independent normalization factors that agreed to within 4%. We used the average of the two

values and obtained the following expressions for the *absolute* transition dipole moment functions:

$$\mu_{e,3^1\Pi\rightarrow A^1\Sigma^+}^{absolute}(R) = 11.05 - 5.55\left(\frac{R_{eq}}{R}\right)^2 \quad (23)$$

and

$$\mu_{e,3^1\Pi\rightarrow X^1\Sigma^+}^{absolute}(R) = 3.40\left(\frac{R_{eq}}{R}\right)^2 - 11.04\left(\frac{R_{eq}}{R}\right)^4 + 12.26\left(\frac{R_{eq}}{R}\right)^6 - 3.88\left(\frac{R_{eq}}{R}\right)^8, \quad (24)$$

where the transition dipole moment is given in Debye. We believe the absolute magnitudes of these functions are accurate to $\sim 15\text{--}25\%$, based on a 5% uncertainty in the determination of the electric field, a 10% uncertainty in determination of the Rabi frequency from the AT splitting lineshapes, and a 10–15% uncertainty in the relative line intensities, especially in the $3^1\Pi \rightarrow A^1\Sigma^+$ fluorescence band, which necessarily had to serve as the calibration point in the present experiment. The relative R dependences of these functions are probably accurate to $\sim 5\text{--}10\%$ within each band.

Our best-fit transition dipole moment functions $\mu_{e,3^1\Pi\rightarrow A^1\Sigma^+}^{absolute}(R)$ and $\mu_{e,3^1\Pi\rightarrow X^1\Sigma^+}^{absolute}(R)$ are plotted in Figs. 10 and 11, respectively, where they are compared to the recent theoretical calculations of Magnier *et al.* [1] and the much earlier calculations of Ratcliff *et al.* [9]. Figure 10 also shows the relative $3^1\Pi \rightarrow X^1\Sigma^+$ transition dipole moment function obtained by Laub *et al.* [25] using calibrated fluorescence alone. It can be seen that the most recent theoretical calculations of Magnier *et al.* are in excellent agreement with the current experimental results, with regard to both the absolute magnitude and the functional dependence of the transition dipole moment functions.

For the $3^1\Pi(19,11,f) \rightarrow A^1\Sigma^+(v',11,e)$ transition, it would be beneficial to be able to record fluorescence to higher v 's of the A state, in order to extend the fitted transition dipole moment function to larger R . Unfortunately, the detection efficiency of the current experimental setup drops quickly in the relevant wavelength range and interference from extraneous fluorescence signals prevented us from extending the measurements into this region.

VI. Conclusions

We have demonstrated that a combination of resolved fluorescence scans with Autler-Townes splitting measurements can be used to determine molecular transition dipole moment functions over broad ranges of internuclear separation R . The particular value of combining the two techniques can be seen in the present case where the transition dipole matrix elements are generally small and the electronic transition dipole moment function is strongly dependent on R . In this case, the AT splitting method can only be used to determine the absolute transition dipole matrix elements for a few of the strongest transitions, whereas the resolved fluorescence technique allows determination of many transition dipole matrix elements, including those for much weaker transitions, but only on a relative scale. The combination of the two techniques allows all matrix elements to be measured absolutely, and consequently theoretical transition dipole moment functions can be tested on an absolute basis.

Acknowledgements

This work was supported by the National Science Foundation grants PHY-0652938 and PHY-0555608.

References

1. S. Magnier, M. Aubert-Frecon, and P. Millie, *J. Mol. Spectrosc.* **200**, 96 (2000).
2. N. W. Carlson, F. V. Kowalski, R. E. Teets, and A. L. Schawlow, *Opt. Commun.* **29**, 302 (1979).
3. G.-Y. Yan, B. W. Sterling, and A. L. Schawlow, *J. Opt. Soc. Am. B* **5**, 2305 (1988).
4. L. Li and R. W. Field, *J. Phys. Chem.* **87**, 3020 (1983).
5. H. Wang, L. Li, A. M. Lyyra, and W. C. Stwalley, *J. Mol. Spectrosc.* **137**, 304 (1989).
6. T.-J. Whang, H. Wang, A. M. Lyyra, L. Li, and W. C. Stwalley, *J. Mol. Spectrosc.* **145**, 112 (1991).
7. J. T. Kim, H. Wang, J. T. Bahns, and W. C. Stwalley, *J. Chem. Phys.* **102**, 6966 (1995).
8. E. Kagi, N. Yamamoto, H. Fujiwara, M. Fukushima, and T. Ishiwata, *J. Mol. Spectrosc.* **216**, 48 (2002).
9. L. B. Ratcliff, D. D. Konowalow, and W. J. Stevens, *J. Mol. Spectrosc.* **110**, 242 (1985).
10. E. Ahmed, A. Hansson, P. Qi, T. Kirova, A. Lazoudis, S. Kotochigova, A. M. Lyyra, L. Li, J. Qi, and S. Magnier, *J. Chem. Phys.* **124**, 084308 (2006).
11. E. H. Ahmed, P. Qi, B. Beser, J. Bai, R. W. Field, J. P. Huennekens, and A. M. Lyyra, *Phys. Rev. A* **77**, 053414 (2008).
12. M. A. Quesada, A. M. F. Lau, D. H. Parker, and D. W. Chandler, *Phys. Rev. A* **36**, 4107 (1987).
13. A. M. F. Lau and W. M. Huo, *Chem. Phys. Lett.* **157**, 108 (1989).
14. J. Qi, G. Lazarov, X. Wang, L. Li, L. M. Narducci, A. M. Lyyra, and F. C. Spano, *Phys. Rev. Lett.* **83**, 288 (1999), Erratum: *Phys. Rev. Lett.* **88**, 229901 (2002).

15. J. Qi, F. C. Spano, T. Kirova, A. Lazoudis, J. Magnes, L. Li, L. M. Narducci, R. W. Field, and A. M. Lyyra, Phys. Rev. Lett. **88**, 173003 (2002).
16. E. Ahmed and A. M. Lyyra, Phys. Rev. A **76**, 053407 (2007).
17. P. R. Berman and R. Salomaa, Phys. Rev. A **25**, 2667 (1982).
18. C. Delsart and J.-C. Keller, J. Physique **39**, 350 (1978).
19. S. Feneuille and M.-G. Schweighofer, J. Physique **36**, 781 (1975).
20. L. Li, P. Qi, A. Lazoudis, E. Ahmed, and A. M. Lyyra, Chem. Phys. Lett. **403**, 262 (2005).
21. A. M. Lyyra, J. Qi, and F. C. Spano, Can. J. Phys. **79**, 547 (2001).
22. J. Qi and A. M. Lyyra, Phys. Rev. A **73**, 043810 (2006).
23. F. C. Spano, J. Chem. Phys. **114**, 276 (2001).
24. M. G. Stepanov, J. Phys. B **32**, 649 (1999).
25. E. Laub, I. Mazsa, S. C. Webb, J. La Civita, I. Prodan, Z. J. Jabbour, R. K. Namiotka, and J. Huennekens, J. Mol. Spectrosc. **193**, 376 (1999), Erratum: J. Mol. Spectrosc. **221**, 142 (2003).
26. R. Stair, W. E. Schneider, and J. K. Jackson, Appl. Opt. **2**, 1151 (1963).
27. D. R. Skinner and R. E. Whitcher, J. Phys. E **5**, 237 (1972).
28. G. Herzberg, *Spectra of Diatomic Molecules* (D. Van Nostrand Company, Inc., Princeton, New Jersey, 1964).
29. University of Waterloo, "LEVEL 8.0: A Computer Program for Solving the Radial Schrödinger Equation for Bound and Quasibound Levels," Report (2007).
30. A. J. Ross, R. M. Clements, and R. F. Barrow, J. Mol. Spectrosc. **127**, 546 (1988).
31. I. Russier-Antoine, A. J. Ross, M. Aubert-Frecon, F. Martin, and P. Crozet, J. Phys. B **33**, 2753 (2000).

32. S. Stenholm, *Foundations of Laser Spectroscopy* (Wiley-Interscience, New York, 1984).
33. S. J. Sweeney, Ph. D. Dissertation, Lehigh University, Bethlehem, Pennsylvania (2008).
34. T. Kirova, Ph.D. Dissertation, Temple University, Philadelphia, Pennsylvania (2005), pages 58-70.
35. J. Sagle, R. K. Namiotka, and J. Huennekens, *J. Phys. B* **29**, 2629 (1996).

Figure Captions

Fig. 1: Experimental setup used in the present experiment. L, F, and ND represent lens, interference filter, and neutral density filter, respectively. Bold arrows depict the laser beam paths, while the double dotted lines depict fluorescence paths.

Fig. 2: (a) Pumping scheme for measuring resolved $3^1\Pi(19,11,f) \rightarrow A^1\Sigma^+(v',11,e)$ and $3^1\Pi(19,11,f) \rightarrow X^1\Sigma^+(v'',11,e)$ fluorescence transitions. (b) Pumping scheme for probing the AT splitting lineshape. Total $3^1\Pi \rightarrow X^1\Sigma^+$ fluorescence is detected with a freestanding PMT with short-pass filters. An actual AT splitting scan (insert) shows the AT lineshape probed in this work.

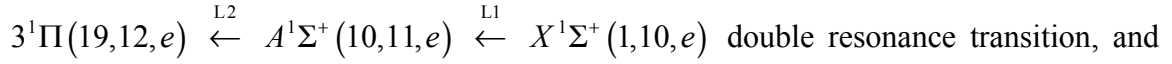
Fig. 3: Resolved NaK $3^1\Pi(19,11,f) \rightarrow A^1\Sigma^+(v',11,e)$ red fluorescence obtained using the pumping scheme $3^1\Pi(19,11,f) \leftarrow A^1\Sigma^+(10,11,e) \leftarrow X^1\Sigma^+(1,12,e)$. Vertical arrows indicate lines of the $3^1\Pi(19,11,f) \rightarrow A^1\Sigma^+(v',11,e)$ series of interest, while other unmarked lines are parts of other sequences that are coincidentally excited. The horizontal arrow shows the range of the potassium resonance lines. Very low transmission through the vapor in this range results in unreliable molecular line intensities that are not used in the analysis.

Fig. 4: Resolved NaK $3^1\Pi(19,11,f) \rightarrow X^1\Sigma^+(v'',11,e)$ violet fluorescence obtained using the pumping scheme $3^1\Pi(19,11,f) \leftarrow A^1\Sigma^+(10,11,e) \leftarrow X^1\Sigma^+(1,10,e)$. Inset: expanded view of the range 4200-4600 Å.

Fig. 5: AT splitting pumping scheme. Levels $|1\rangle$, $|3\rangle$, and $|5\rangle$ are the initial, intermediate, and final states of the two-laser OODR pump scheme. Level $|6\rangle$ corresponds to all possible levels, other than level $|3\rangle$ and levels of the ground state $X^1\Sigma^+$, that can be reached by radiative decay from the $3^1\Pi$ state. Level $|2\rangle$ corresponds to all rovibrational levels in the ground state other than level $|1\rangle$.

Fig. 6: AT lineshape for the (a) $3^1\Pi(19,11,f) \leftarrow A^1\Sigma^+(10,11,e)$ and (b) $3^1\Pi(19,11,f) \leftarrow A^1\Sigma^+(9,11,e)$ transitions. Thin solid lines represent calculated lineshapes using $\Omega_{35} = 1.596 \times 10^9 \text{ s}^{-1}$ (254 MHz), $\Omega_{13} = 2.213 \times 10^8 \text{ s}^{-1}$ (35.22 MHz), $\gamma_{13}^c = 1.00 \times 10^8 \text{ s}^{-1}$, $\gamma_{15}^c = 0.75 \times 10^8 \text{ s}^{-1}$, and $\gamma_{35}^c = 0.50 \times 10^8 \text{ s}^{-1}$ in part (a), and $\Omega_{35} = 8.796 \times 10^8 \text{ s}^{-1}$ (140 MHz), $\Omega_{13} = 3.221 \times 10^8 \text{ s}^{-1}$ (51.26 MHz), $\gamma_{13}^c = 1.20 \times 10^8 \text{ s}^{-1}$, $\gamma_{15}^c = 0.60 \times 10^8 \text{ s}^{-1}$, and $\gamma_{35}^c = 0.20 \times 10^8 \text{ s}^{-1}$ in part (b). For the calculations of the AT lineshape, the transit relaxation rate $\Gamma_t = 3.3 \times 10^6 \text{ s}^{-1}$ was used, and the total radiative decay rates out of levels 3, 6, and 5 were taken to be $\Gamma_3 = \Gamma_6 = 4.51 \times 10^7 \text{ s}^{-1}$ and $\Gamma_5 = 3.72 \times 10^7 \text{ s}^{-1}$.

Fig. 7: a) Power dependence of the measured splitting due to the Autler-Townes effect in the



b) representative scans. It can be seen that the measured splittings scale linearly with the electric field ($\text{Power}^{1/2}$) of the coupling laser L2.

Fig. 8: Experimental and calculated intensities for $3^1\Pi(19,11,f) \rightarrow A^1\Sigma^+(\nu',11,e)$ transitions.

Transitions to $\nu_{lower} = \nu' = 13, 14, \text{ and } 15$, marked by a horizontal arrow, are unable to be used in the analysis, since light at these particular wavelengths experiences near-zero transmission through the vapor due to potassium resonance line absorption.

Fig. 9: Experimental and fitted intensities for $3^1\Pi(19,11,f) \rightarrow X^1\Sigma^+(\nu'',11,e)$ transitions.

$\nu_{lower} = \nu''$. Inset: intensities magnified by factor of 20.

Fig. 10: Solid line: the absolute experimental NaK $3^1\Pi \rightarrow A^1\Sigma^+$ transition dipole moment function versus internuclear separation obtained in the present work

$$[\mu_{e,3^1\Pi \rightarrow A^1\Sigma^+}^{absolute}(R) = 11.05 - 5.55(R_{eq}/R)^2 \text{ Debye}]. \text{ Dashed line: theoretical transition dipole}$$

moment function from Ref. [1]. Dotted line: theoretical transition dipole moment function from Ref. [9].

Fig. 11: Thick solid line: the absolute experimental NaK $3^1\Pi \rightarrow X^1\Sigma^+$ transition dipole moment

function versus internuclear separation obtained in the present work

$$[\mu_{e,3^1\Pi \rightarrow X^1\Sigma^+}^{absolute}(R) = 3.40(R_{eq}/R)^2 - 11.04(R_{eq}/R)^4 + 12.26(R_{eq}/R)^6 - 3.88(R_{eq}/R)^8$$

Debye]. Dashed line: theoretical transition dipole moment function from Ref. [1].

Dotted line: theoretical transition dipole moment function from Ref. [9]. Thin solid line:

relative transition dipole moment function from Ref. [25], normalized to theory at $R =$

4.76 Å.

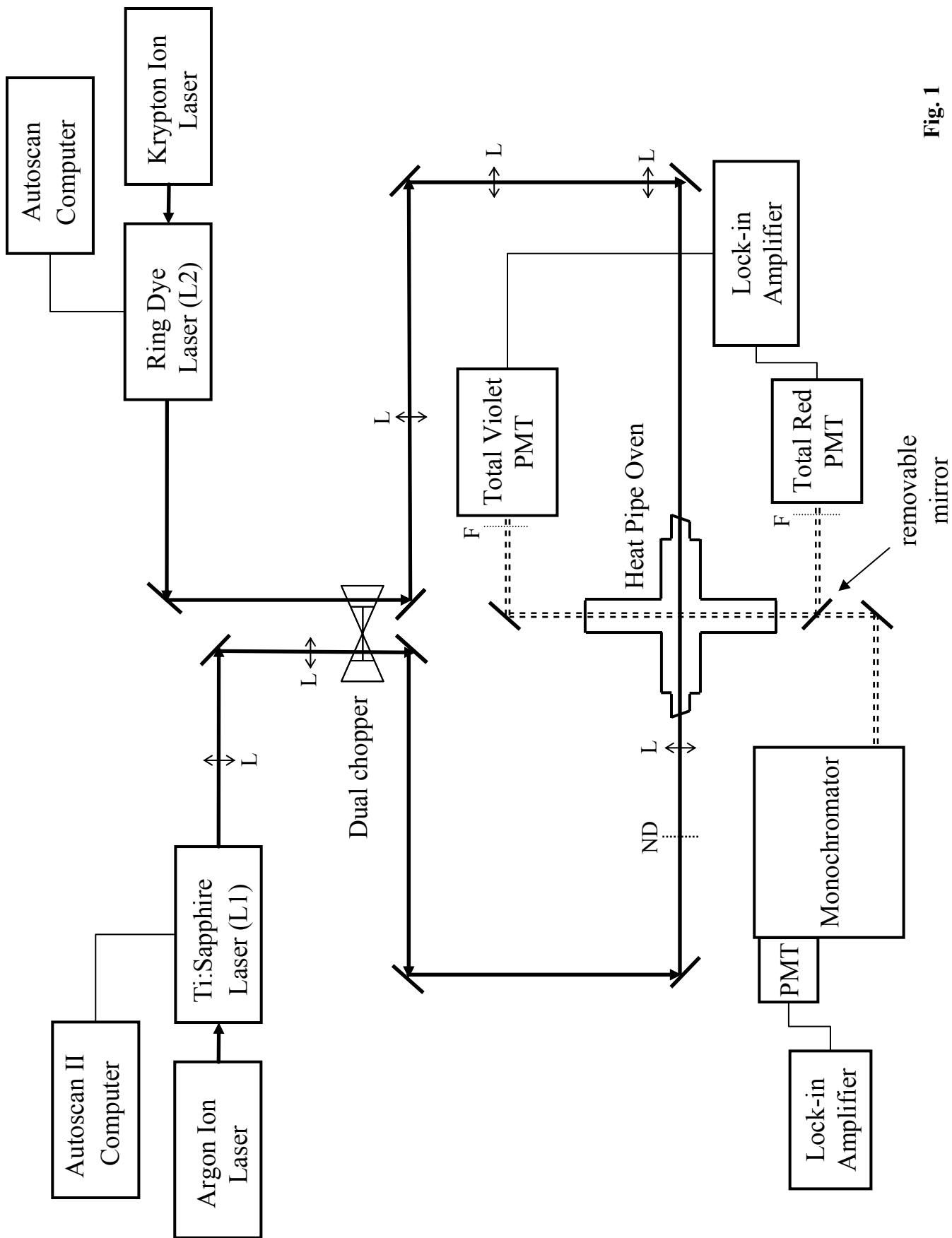


Fig. 1

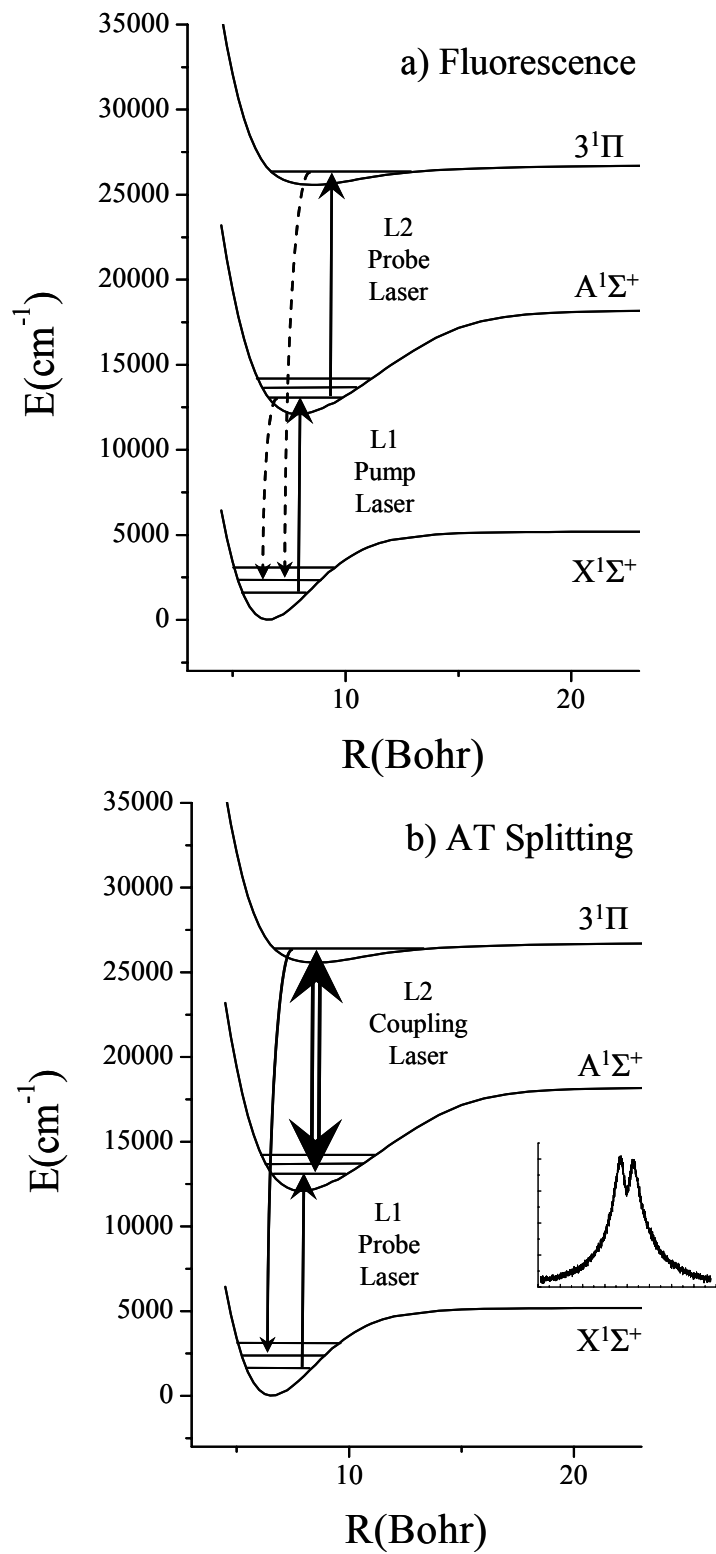


Fig. 2

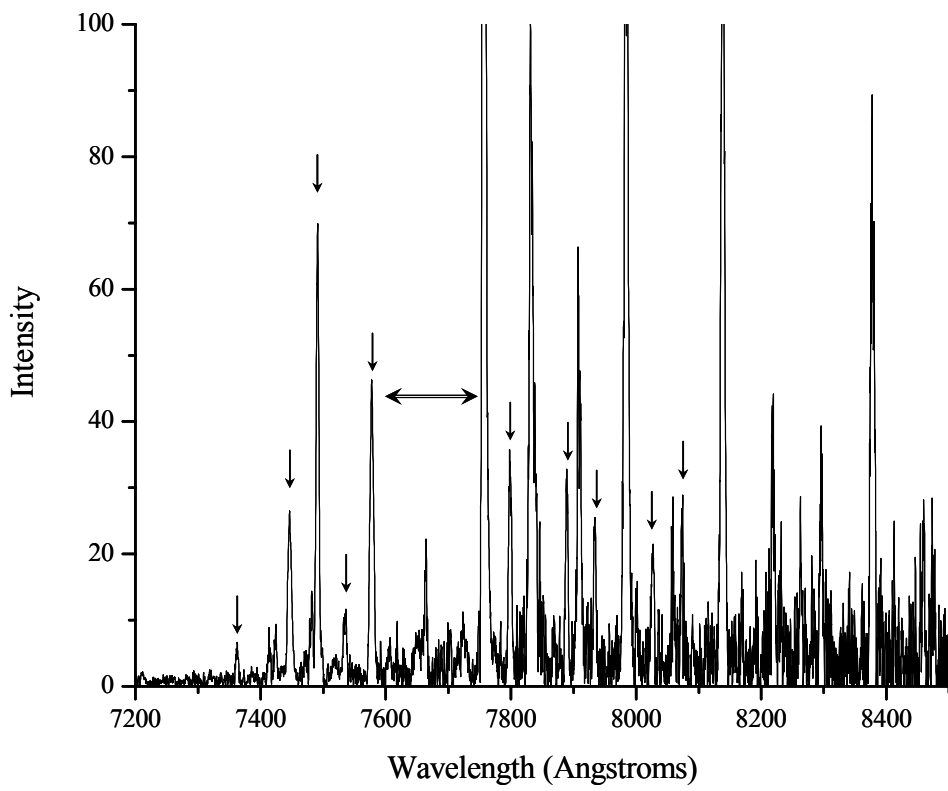


Fig. 3

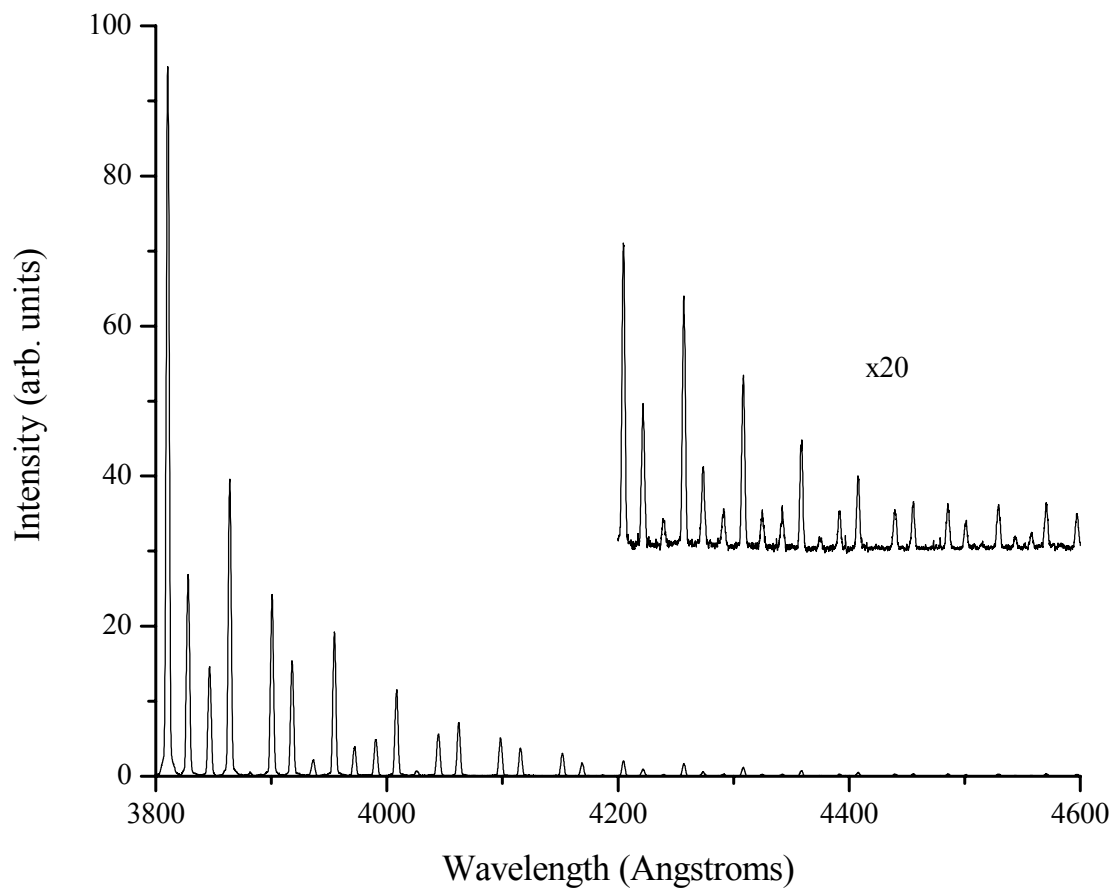


Fig. 4

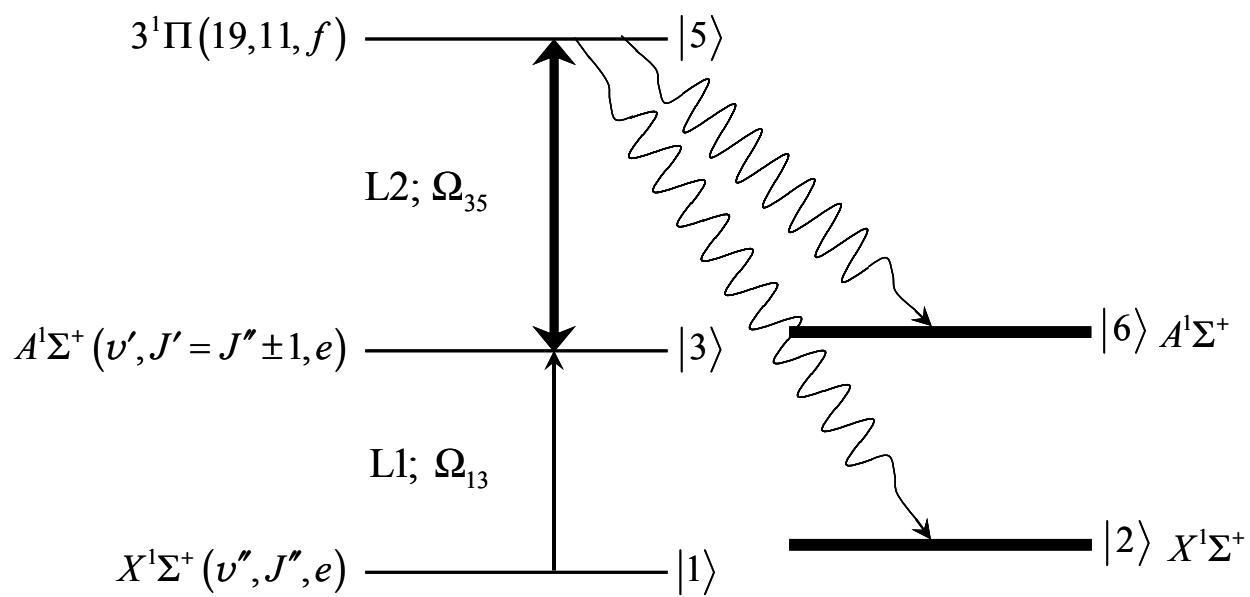


Fig. 5

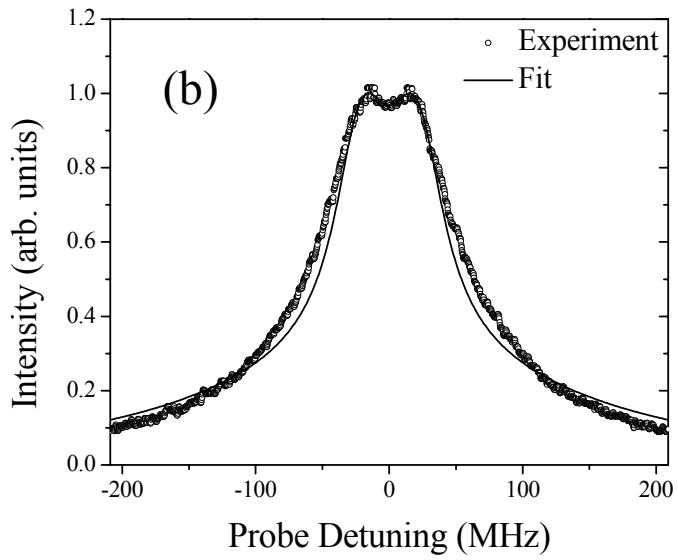
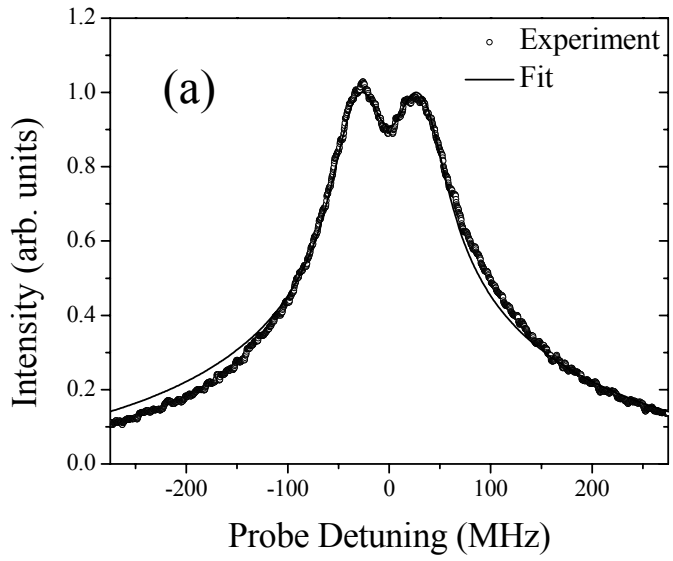


Fig. 6

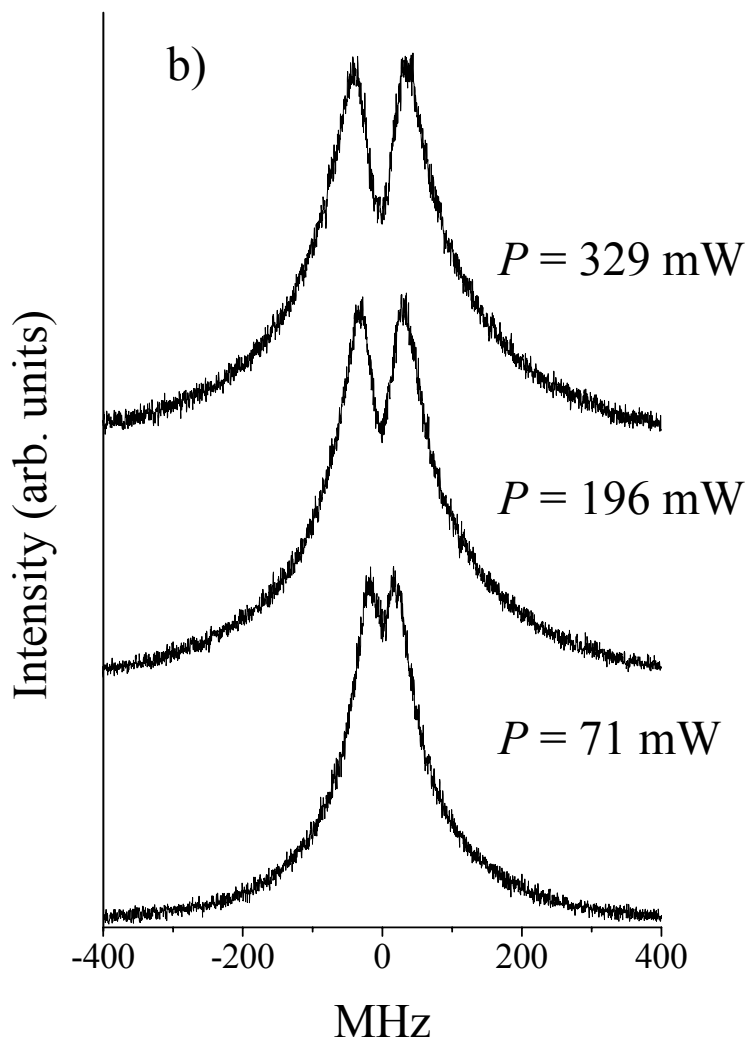
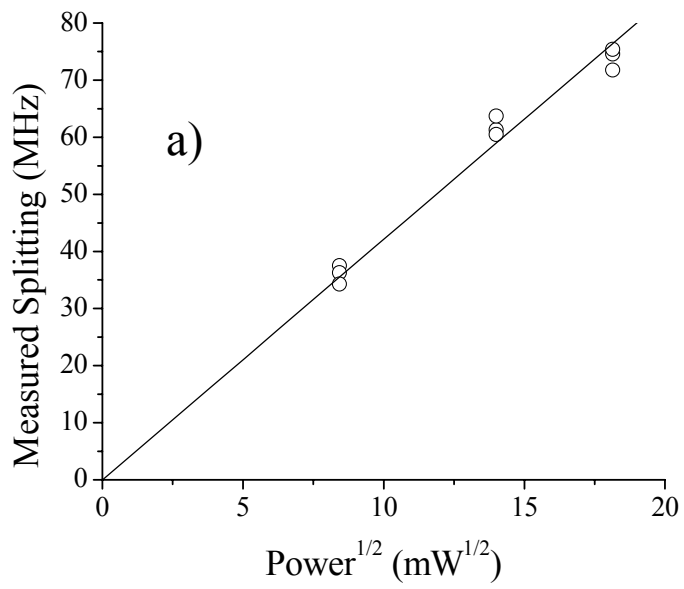


Fig. 7

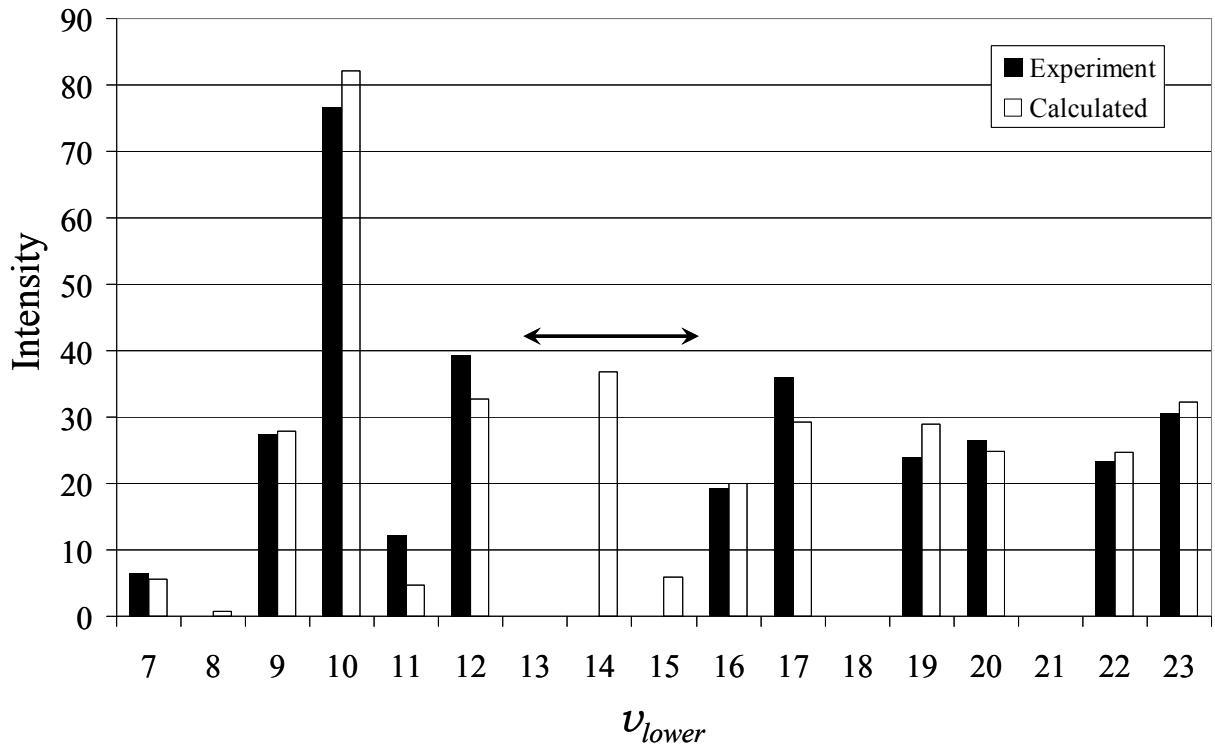


Fig. 8

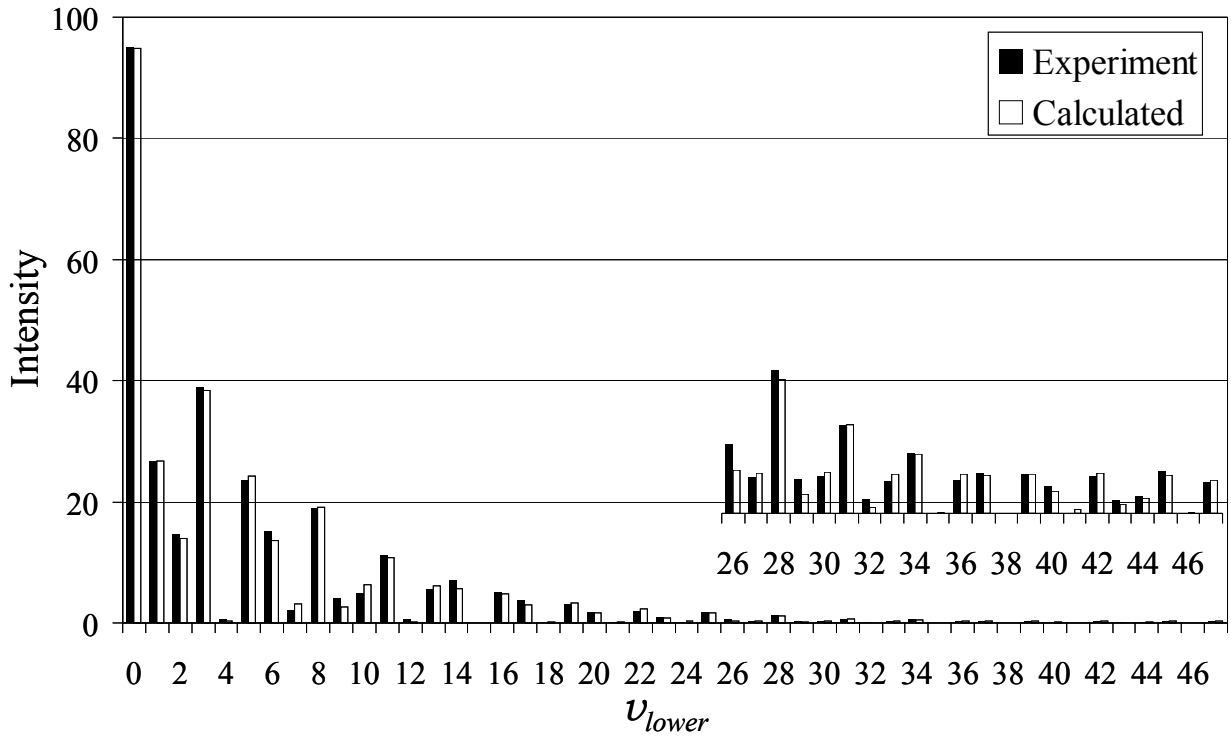


Fig. 9

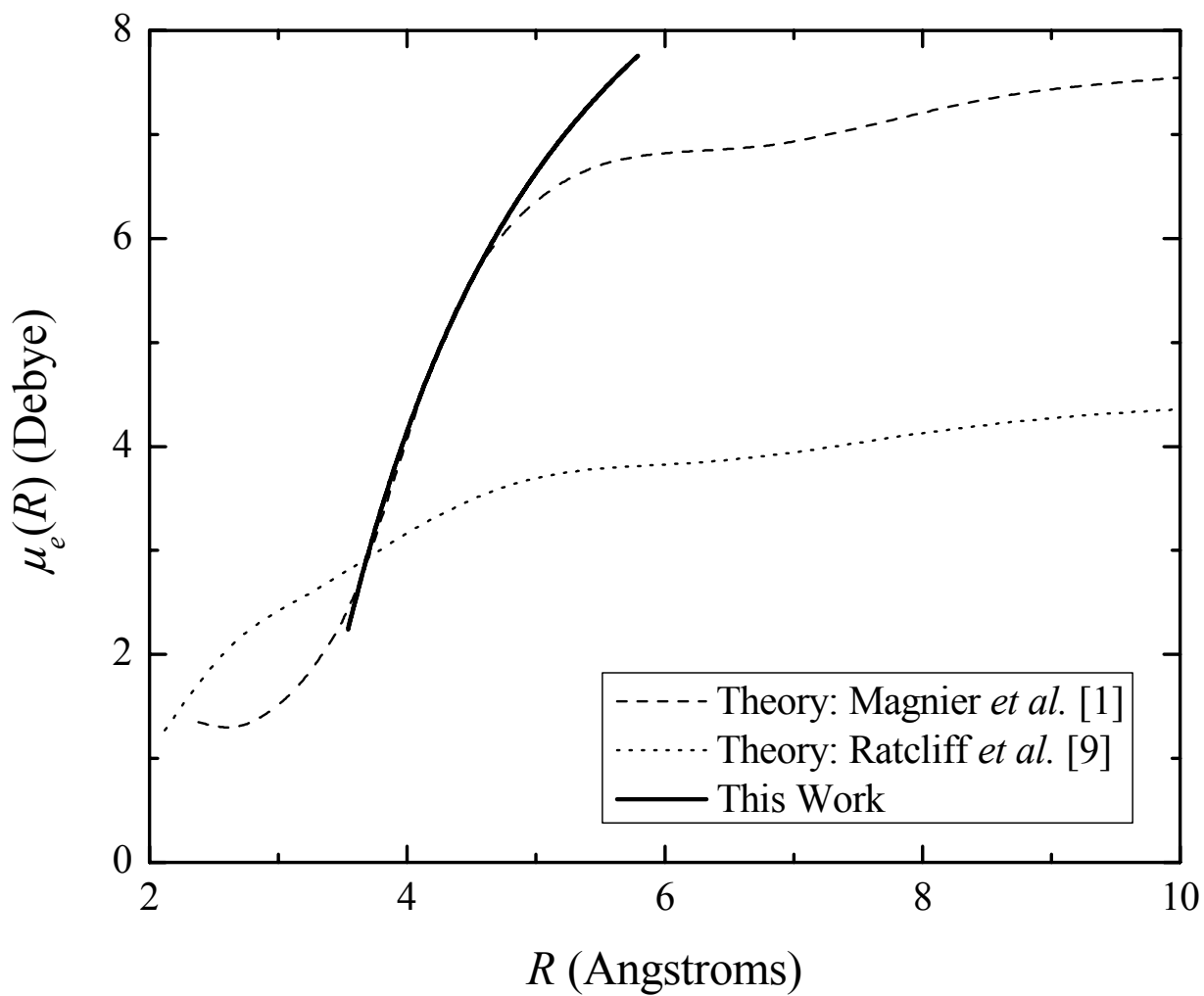


Fig. 10

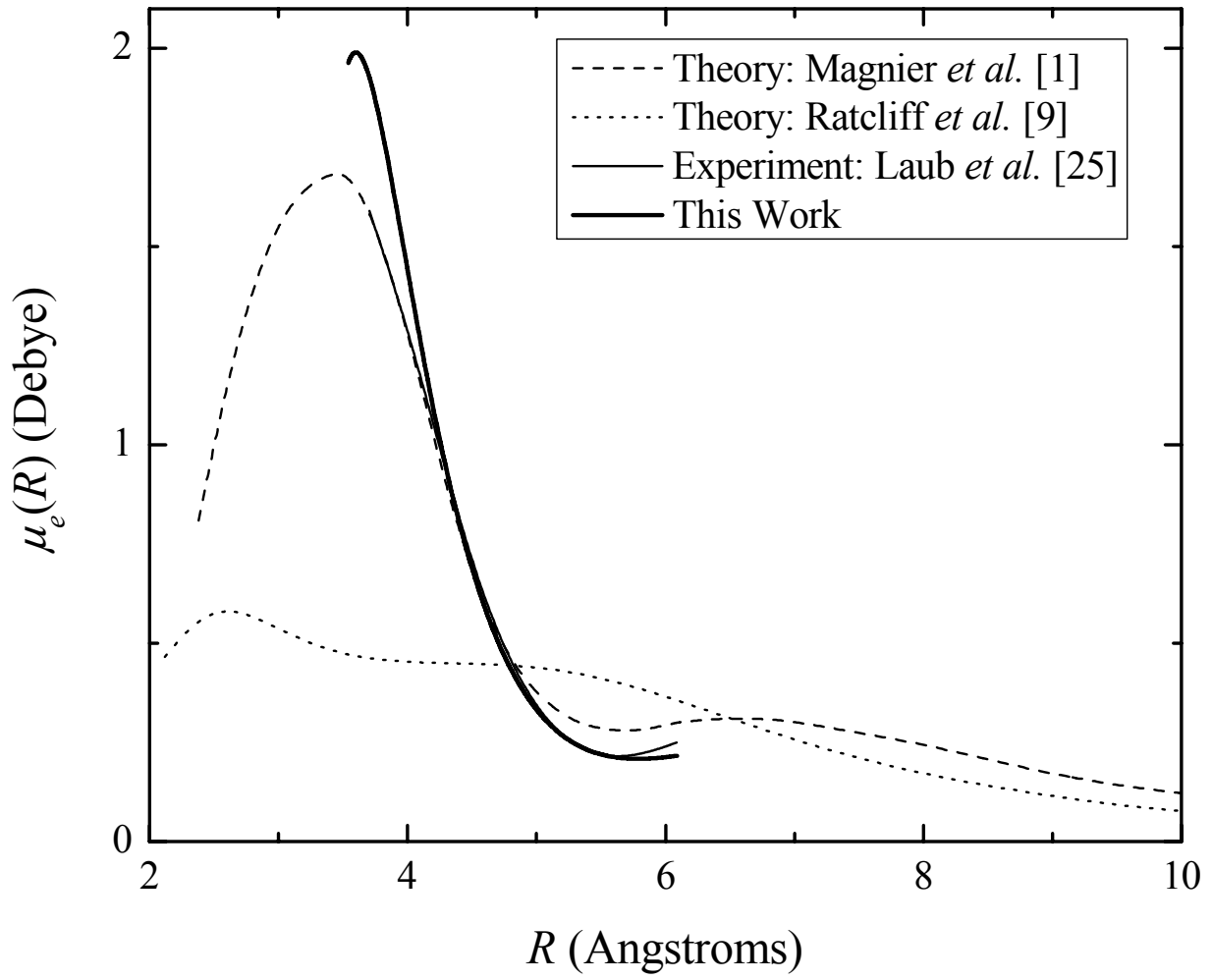


Fig. 11